ACSNANO

www.acsnano.org

ARTICLE

Armored Droplets as Soft Nanocarriers for Encapsulation and Release under Flow Conditions

François Sicard* and Jhoan Toro-Mendoza

Cite This: https://doi.org/10.1021/acsnano.1c00955

Read Online

ACCESS | Metrics & More | Article Recommendations | Supporting Information

ABSTRACT: Technical challenges in precision medicine and environmental remediation create an increasing demand for smart materials that can select and deliver a probe load to targets with high precision. In this context, soft nanomaterials have attracted considerable attention due to their ability to simultaneously adapt their morphology and functionality to complex ambients. Two major challenges are to precisely control this adaptability under dynamic conditions and provide predesigned functionalities that can be manipulated by external stimuli. Here, we report on the computational design of a distinctive class of soft nanocarriers, built from armored nanodroplets, able to selectively encapsulate or release a probe load under specific flow conditions. First, we describe in detail the mechanisms at play in the formation of *pocket-like* structures in armored nanodroplets and their stability under external flow. Then we use that knowledge to test the capacity of these pockets to yield flow-assisted encapsulation or expulsion of a probe load. Finally, the rheological properties of these nanocarriers are put into perspective with those of delivery systems employed in pharmaceutical and cosmetic technology.

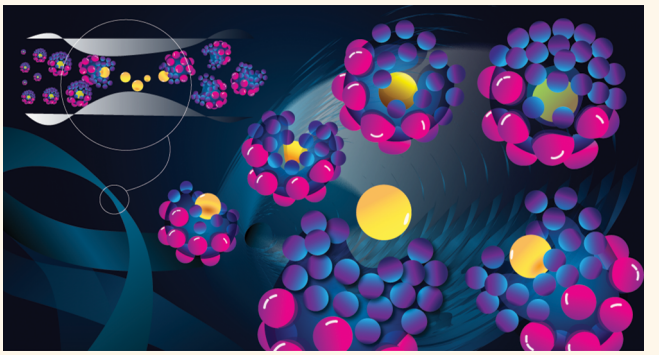

KEYWORDS: *smart materials, nanocarrier, Pickering emulsions, flow-assisted encapsulation, dissipative particle dynamics*

Considerable attention has been devoted to the design, characterization, and development of nanocarriers built on smart materials due to their potential in targeted-oriented active molecule delivery in biological environments[1] and their active role in environmental remediation strategies.[2] This includes soft smart material and soft robotic technology platforms that can be sufficiently miniaturized and demonstrate flexible and adaptative architecture in complex ambients.[3,4] Materials that fall into this category include but are not limited to structured liquids,[3] shape-memory alloys and polymers,[5] stimulus-responsive hydrogels,[6] and carbon nanotubes.[7]

The morphological and physicochemical properties of soft nanomaterials provide advantages that enable the design of autonomous nanoscale devices that can more closely mimic or interact with biological structures with stimulus-responsive characteristics. In this context, emulsions stabilized with nanoparticles (NPs), also know as Pickering emulsions,[8] offer real advantages in a wide range of fundamental[9−13] or industrial and medical applications.[14−16] They can serve as a template for autonomous platforms that are able to change their shape and adopt different functionalities as a result of morphological transformation obtained *via* interfacial self-assembly and cross-linking,[17,18] dynamical control of the NP distribution with electric or magnetic fields,[19−26] or dynamical control of the fluidic environment,[27,28] among other techniques.

NP-coated droplets have been intensively used as drug-delivery vehicles in topical medication,[29] where their surfactant-free character makes them attractive for different applications since surfactants often produce adverse effects, such as irritation and hemolytic disturbances.[30,31] They can serve as ideal compartments for reactions catalyzed by NPs attached at the oil−water interfaces[32−35] and can be used in bacterial recognition technologies.[36,37] Another important and useful advantage of NP-coated droplets over conventional

Received: February 1, 2021
Accepted: July 13, 2021

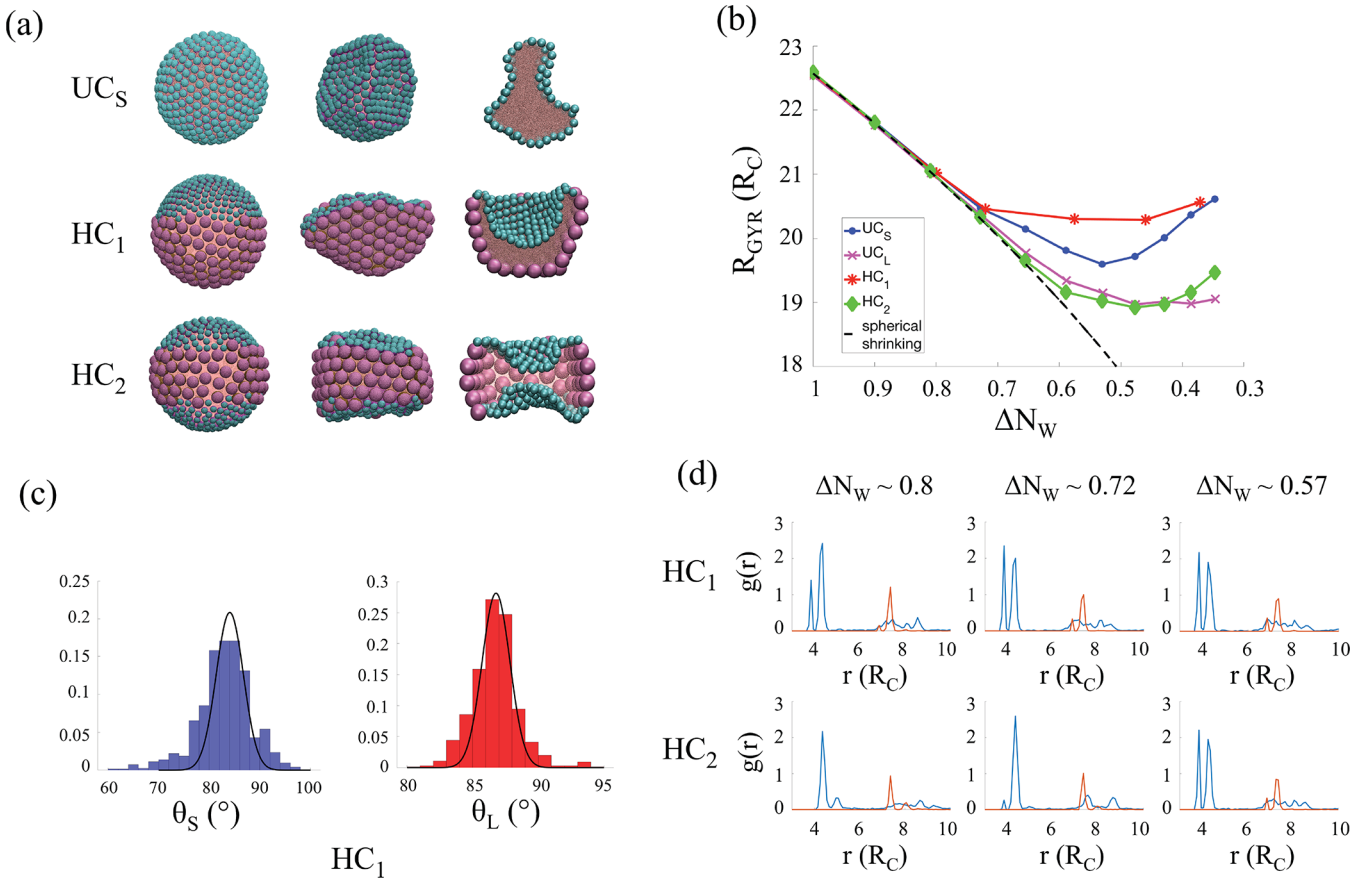

Figure 1. Formation of pocket-like structures. (a) Simulation snapshots representing the initial (left) and final (center) water in oil droplets armored with different nanoparticle surface coverages, obtained from the evaporation process: uniformly covered droplets with small NPs (UC_S) and heterogeneously covered droplets with either each hemisphere covered with small or large NPs (HC_1) or three distinct layers made of small−large−small NPs (HC_2). The cross-sectional view of each system is also shown (right). Cyan and purple spheres represent the small and large Janus NPs, respectively. The detailed structure of the NPs is shown in Figure S1a in the SI. Pink spheres represent water beads. The oil molecules surrounding the system are not shown for clarity. (b) Evolution of the radius of gyration, R_{GYR}, of UC_S, UC_L, HC_1, and HC_2, as a function of the dimensionless parameter $\Delta N_W = N_W/N_W^{(0)}$. N_W represent the number of water beads that remain in the droplet after each removal, and $N_W^{(0)}$ is the initial number of water beads. The statistical errors are estimated as one standard deviation from the average obtained for equilibrated trajectories and are always smaller than the symbols. The dashed lines represent the spherical-shrinking regime defined as $R_{GYR} \approx (\Delta N_W)^{1/3}$. (c) Three-phase contact angle distribution of small (blue) and large (red) NPs for HC_1 after the last pumping/equilibration iteration ($\Delta N_W \approx 0.35$). (d) Evolution of the radial distribution function, $g(r)$, with r the distance between the center of the NPs, of small (blue) and large (red) NPs for HC_1 (b) and HC_2 (c).

surfactant-stabilized systems is their enhanced stabilization against coalescence[38] and their smaller environmental footprint.[27]

While tremendous progress has been made in highly controlled particle-based microfluidic technology[39,40] and NP assembly at fluid interfaces,[41,42] the inherent limitation in experimental resolution eludes direct access to local observables, such as the particles' three-phase contact angle distribution and the details of the particles' interfacial network, which present complex geometries.[43] This information can be accessed by numerical simulations.[38,44−46] Predicting and controlling this interfacial arrangement under external stimuli to advance the design of the next generation of smart nanocarriers, incorporating soft-matter architectures for precision medicine, is even more challenging.

The recent experimental report by Rozynek *et al.*[12] on controlled deformation of micron-sized Pickering droplets using electric fields encouraged us to propose strategies for design, analogous to coated nanodroplets under flow. To further contribute in that direction, we report here on the computational design of a distinctive class of soft nanocarriers inspired by Pickering nanoemulsion systems, which can have potential in targeted-oriented active molecule encapsulation and release under specific flow conditions. Those conditions are consistent with the high-shear regime of spreading topical medication on the skin and the transport of targeted carriers in pathological alterations of the vascular system, both of them being successfully reproduced in microfluidic devices.[47−49] Dissipative particle dynamics (DPD) is employed as a mesoscopic simulation method[50] with two aims: (1) to describe in detail the formation of *pocket-like* structures in NP-coated nanodroplets and their stability under specific flow conditions and then (2) to test the capacity of the formed pockets to encapsulate or expel a probe load.

Water nanodroplets coated with spherical NPs with different diameters and immersed in an organic solvent are considered. The coating is formed by Janus NPs, *i.e.*, particles whose surface shows two distinct wetting properties on each half,[51,52] whose initial three-phase contact angles result in maximum adsorption energy at the fluid−fluid interface.[53] We first

https://doi.org/10.1021/acsnano.1c00955
ACS Nano XXXX, XXX, XXX−XXX

characterize the interfacial properties of the system (three-phase contact angles and diffusion coefficient of the individual NPs, decrease of interfacial tension). We study the role of the NP surface coverage and the interfacial mechanisms at play in the surface mechanical instabilities responsible for the deformation of the armored nanodroplets, when the volume of the droplet is reduced. In particular, we observe in detail the formation of crater-like depressions with selective geometry, which can structurally favor the loading of a probe load. We then investigate the dynamical response of these *pocket-like* structures subjected to homogeneous shear flow using nonequilibrium simulations and the SLLOD equations of motion. Under specific conditions, we observe the formation of long-lived anisotropic structures, characteristic of a jammed particle coverage at the liquid−liquid interface. Furthermore, we examine the capacity of the system to control the flow-assisted encapsulation or expulsion of a probe load, which depends on the interplay between NP surface coverage, the level of buckling, and the shear flow conditions. Finally, we discuss the plausibility of applying the latter predictions to systems in the micron scale, of interest but not limited to pharmaceutical and cosmetic technology.

RESULTS AND DISCUSSION

System Characteristics. We first give the characteristics and assess the interfacial properties of the NP-coated droplets considered in this work. In Figure 1a we show representative snapshots of the water emulsion nanodroplets in an organic solvent (decane) stabilized with Janus NPs. The scaled temperature in the DPD framework is equivalent to 298.73 K. The details of the numerical parametrization and NP structures are given in the Methods section and the Supporting Information (SI). The configurations differ by the size of the NPs and the characteristics of the surface coverage. We consider small (S) and large (L) NPs with diameters $d_S \approx 2.2$ nm and $d_L \approx 4.5$ nm, whose diffusion coefficients measured on a planar decane/water interface are $D_S \approx (4.7 \pm 3.1) \times 10^{-7}$ cm^2 s^{-1} and $D_L \approx (1.8 \pm 0.7) \times 10^{-7}$ cm^2 s^{-1}, respectively (see Methods and Figure S1c in the SI).

The NPs are originally located at the surface of the emulsion nanodroplets of diameter $d_D \approx 45$ nm. Similar NP surface coverage $\phi \approx 0.8$ is considered on the armored nanodroplets.[44,54] This yields similar initial three-phase contact angles $\theta_S \approx 84.1 \pm 2.7°$ and $\theta_L \approx 86.8 \pm 1.1°$ for the small and large NPs, respectively (see Methods and Figure S1b in the SI), in qualitative agreement with simulations[38,55,56] and experimental observations.[57] From the error bars estimated, it is observed that the small NPs are more sensitive to thermal fluctuations at the interface compared to the large ones, characteristic of the increase of the adsorption energy with the particle radius.[58−60] We also measure the decrease of the interfacial tension, $\Delta\gamma_S$ and $\Delta\gamma_L$, for small and large NPs at planar interfaces for similar NP surface coverage (see Methods). We obtain $\Delta\gamma_S = \gamma_0 - \gamma_S \approx 5.1$ mN·m^{-1} and $\Delta\gamma_L = \gamma_0 - \gamma_L \approx 2.2$ mN·m^{-1}, with $\gamma_0 \approx 51.7$ mN·m^{-1} being the interfacial tension for a planar decane/water interface,[46,56] and $\gamma_{S,L}$ the interfacial tension when the interface is covered with small or large NPs, respectively. In particular, large NPs have less effect on the reduction of the interfacial tension and are less diffusive than smaller ones, in qualitative agreement with simulations[60] and experimental observations.[61] As we will see in the following sections, the difference in mobility and size of the NPs play a key role in the pocket formation.

Formation of Pocket-like Structures. To obtain the desired *pocket-like* morphology at the surface of the nanodroplets, which would eventually favor the loading of a probe load, the volume of the droplets is systematically reduced, by iteratively pumping a small constant proportion of water molecules out of the droplets and letting the systems equilibrate between each iteration (see details in the SI). The systems present dimples and cups at the droplet interface followed by the formation of crater-like depressions, characteristic of the buckling instability.[44,62,63] This process is physically equivalent to a process of solubilization of the dispersed phase into the solvent.[44,62] We arbitrarily stop the pumping when the number of water molecules constituting the droplets reaches the value $\Delta N_W = N_W/N_W^{(0)} \approx 0.35$, where $N_W^{(0)}$ and N_W are the initial number of water beads and the number of water beads remaining in the droplets, respectively.

In Figure 1b, we show the evolution of the radius of gyration of the emulsion nanodroplets, R_{GYR}, as a function of the dimensionless parameter ΔN_W. We initially consider spherical droplets whose surface is either uniformly covered (UC) with NPs of identical diameter or heterogeneously covered (HC) with NPs of different diameters segregated on each side. Specifically, UC_S (respectively UC_L) is solely covered with small (respectively large) NPs, as shown in Figure 1a. HC_1 and HC_2 have each hemisphere covered with small and large NPs or three distinct layers made of small−large−small NPs, respectively (*cf.* Figure 1a). When $\Delta N_W > 0.75$, the radius of gyration of the four systems follows a similar evolution, regardless of the NP coverage (UC or HC), characteristic of a spherical-shrinking regime, $R_{GYR} \approx (\Delta N_W)^{1/3}$ (dashed line in Figure 1b). When $\Delta N_W < 0.75$, the systems follow different transitions from spherical shrinking to buckling, depending on the characteristics of the NP interfacial packing originating from the difference in surface coverage.[64] This transition happens when the NP monolayer becomes close to its maximum packing, as observed with the evolution of the radial distribution function $g(r)$, with r being the distance between the center of the NPs, shown in Figure 1d and Figures S2 in the SI. The radial distribution function (rdf) has been intensively used to study the evolution of the ordering of NP aggregates in Pickering emulsions, consistent with experimental observations. In particular, UC_S and UC_L show different morphological evolutions when ΔN_W decreases, with UC_S entering the buckling regime at larger ΔN_W than UC_L, in qualitative agreement with the numerical work of Gu *et al.*[63] Finally, below $\Delta N_W \approx 0.45$, R_{GYR} increases as the droplets can be described as half-sphered.

The structures of the armored nanodroplets obtained after the last pumping/equilibration iteration are shown in Figure 1a (central panel). Visual inspection shows different folding morphologies, depending on the characteristics of the NP coverage. Unlike UC, where crater-like depressions form evenly at the interface under the effect of a compressive surface stress, we observe the formation of well-localized crater-like depressions in heterogeneously covered systems (HC_1 or HC_2). This latter evolution depends on the localization of the interfacial areas covered with small or large NPs. Notably, we observe the crater-like depressions form in the interfacial areas covered with the smallest NPs, where maximum packing of the interfacial network is achieved quicker and the interfacial tension is lower than those measured for larger NPs.

https://doi.org/10.1021/acsnano.1c00955
ACS Nano XXXX, XXX, XXX−XXX

Table 1. Measure of the Mean (μ) and Standard Error (σ) of the Three-Phase Contact Angle Distribution in UC and HC Droplets in the Initial ($\Delta N_W \approx 1.0$) and Final ($\Delta N_W \approx 0.35$) Configurations

ΔN_W		UC_S	UC_L	HC_1	HC_2
1.0	(S)	84.1 ± 2.7°		84.1 ± 2.7°	84.1 ± 2.7°
	(L)		86.8 ± 1.1	86.8 ± 1.1°	86.8 ± 1.1°
0.35	(S)	82.9 ± 5.9°		82.8 ± 6.0°	82.4 ± 6.4
	(L)		83.6 ± 9.9°	86.7 ± 1.9°	87.0 ± 1.8

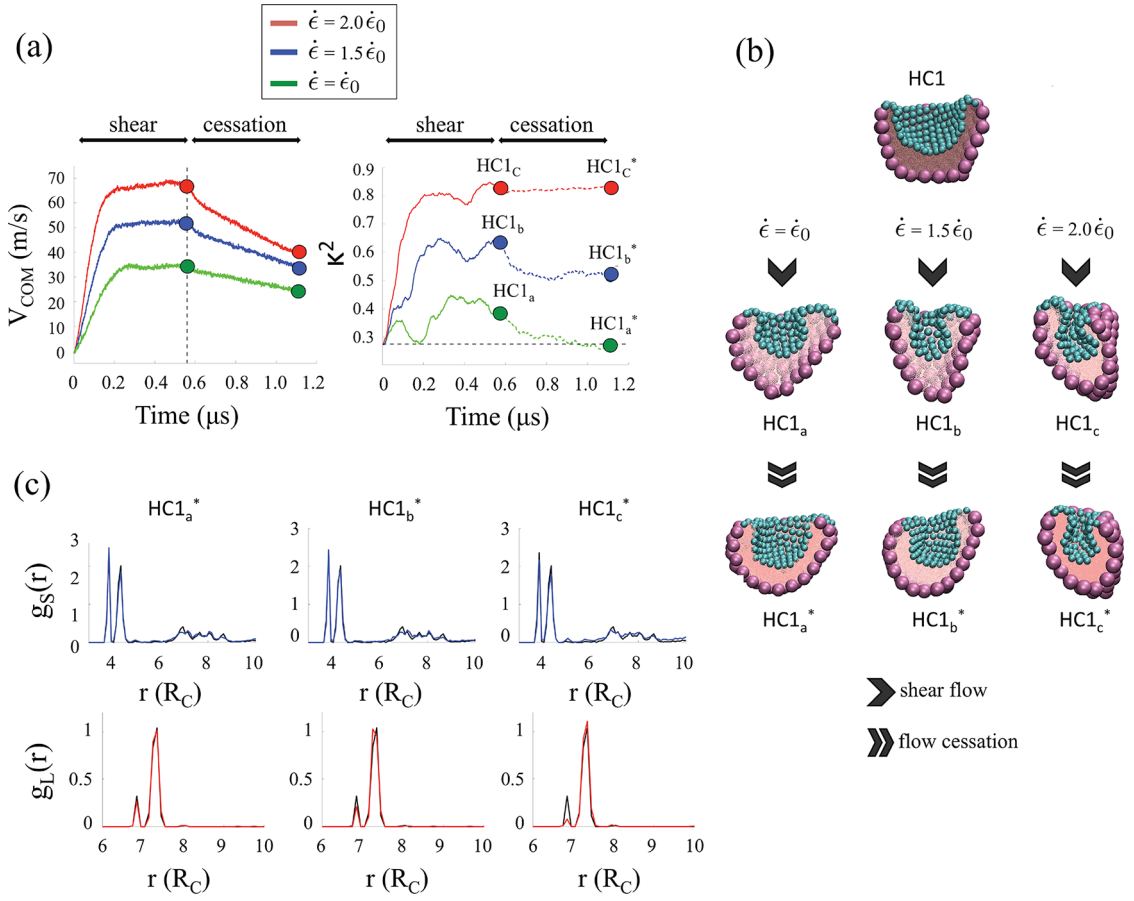

Figure 2. Dynamical response under shear flow. (a) Temporal evolution of the velocity center of mass V_{COM} and the relative shape anisotropy κ^2 of HC_1 subjected to shear flow and after abrupt shear cessation for three different values of the shear rate $\dot{\epsilon}$. The shear flow is continuously applied for a time duration $\Delta t \approx 0.6$ μs before it is abruptly stopped and the structure relaxes for another $\Delta t \approx 0.6$ μs. (b) Representative snapshots of the armored nanodroplets obtained just before the flow cessation ($t \approx 0.6$ μs) and at the end of the simulation ($t \approx 1.2$ μs). Cyan and purple spheres represent the small and large Janus NPs, respectively. The detailed structure of the NPs is shown in Figure S1a in the SI. Pink spheres represent water beads. The oil molecules surrounding the system are not shown for clarity. (c) Radial distribution function, $g_S(r)$ and $g_L(r)$, with r being the distance between the center of the NPs, of small (blue) and large (red) NPs for $HC1^*_{a,b,c}$. The corresponding radial distribution functions measured before the shear flow is applied (HC1) are shown in black color for comparison.

The properties of the interfacial layers are quantitatively assessed *via* the analysis of the distribution of the three-phase contact angles, $\theta_C^{(S)}$ and $\theta_C^{(L)}$, of small and large NPs, respectively. As shown in Figure S1b in the SI, $\theta_C^{(S)}$ and $\theta_C^{(L)}$ follow Gaussian distributions in the initial configurations ($\Delta N_W \approx 1$), where the shape of the droplets is spherical. When the volume of UC_S and UC_L is reduced, $\theta_C^{(S)}$ and $\theta_C^{(L)}$ uniformly evolve from Gaussian to skewed unimodal distributions, in line with previous work.[44] The values of the respective means, μ_S and μ_L, and standard deviations, σ_S and σ_L, for small and large NPs, respectively, are shown in Table 1. Whereas the contact angle distributions show a single peak centered at the same value as the one measured for the initial configuration, σ_S and σ_L show significant variations when the volume of the droplets is reduced, characteristic of the skewness of the distribution and the decrease of the NP−NP distance (*cf.* Figure S2 in the SI). When the volume of HC_1 and HC_2 is reduced, on the other hand, we observe significant differences in the evolution of the distributions of $\theta_C^{(S)}$ and $\theta_C^{(L)}$, due to the heterogeneity in NP size and surface coverage. In particular, the distribution of $\theta_C^{(L)}$ is similar to the one measured in the initial configuration, while the distribution of $\theta_C^{(S)}$ shows large variability, similar to the one measured in UC_S, during the buckling transition, originating from the difference in packing of the monolayer at the droplet interface, as shown in Figure 1c.

From the analysis above, we showed that the formation of well-localized *pocket-like* structures at the surface of the NP-coated droplets can be selectively controlled *via* the

https://doi.org/10.1021/acsnano.1c00955
ACS Nano XXXX, XXX, XXX−XXX

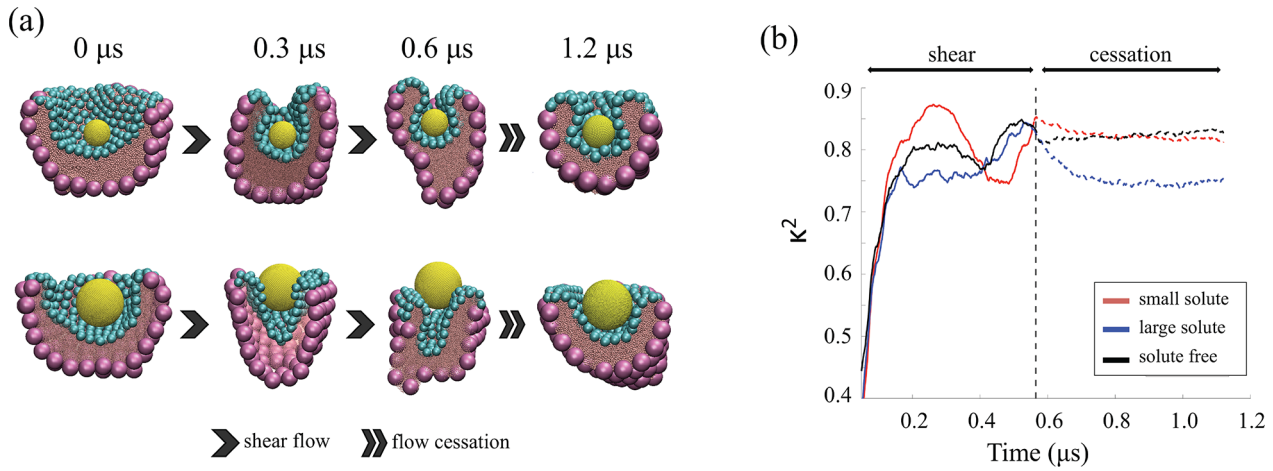

Figure 3. Encapsulation and release of the probe load. (a) Representative snapshots of the structural morphology of HC1 preliminary loaded with small (S) and large (L) hydrophobic spherical solute of diameter $d_S \approx 7.7$ nm (top panel) and $d_L \approx 15.4$ nm (bottom panel), respectively, at different simulation stages. Cyan and purple spheres represent the small and large Janus NPs, respectively. The detailed structure of the NPs is shown in Figure S1a in the SI. Pink and gold spheres represent water and solute beads. The oil molecules surrounding the system are not shown for clarity. (b) Representative temporal evolution of the relative shape anisotropy, κ^2, of HC_1 loaded with small and large solute, subjected to shear flow ($\dot{\epsilon} = 2 \times \dot{\epsilon}_0$) and after abrupt shear cessation. The shear flow is continuously applied for a time duration $\Delta t \approx 0.6$ μs before it is abruptly stopped and the structure relaxes for another $\Delta t \approx 0.6$ μs. The evolution of κ^2 for the free system is shown for comparison.

solubilization/evaporation of the disperse phase and with the use of heterogeneous NP layer coverage at the surface of the droplets. This evolution results from the interplay between thermodynamic and steric effects at the liquid/liquid interface, with the difference in NP adsorption energy, interfacial tension, and interfacial packing, between small and large NPs. Moreover, the formation of the *pocket-like* depressions is observed to be primarily controlled by the reorganization of the small NPs at the surface of the heterogeneously coated droplets. The characteristic of the NP interfacial layer can be further tuned to control the size and the number of *pocket-like* depressions that can form in each hemisphere of the NP-coated droplets.

Dynamical Response under Shear Flow. Thereafter, we investigate the structural response of the *pocket-like* structures, as obtained from volume reduction of the armored droplet, subjected to shear flow of the surrounding fluid using the SLLOD algorithm[65,66] coupled with Lee−Edwards periodic boundary conditions[67] (see Methods). We focus our analysis on HC_1, whose structural morphology is more likely to yield better loading of a probe load (*cf.* Figure 1a). The minimum value for the shear rate, $\dot{\epsilon}_0 \approx 0.9$ ns^{-1}, is set to the value for which the initial structure starts showing significant deformations. The system is first stressed under a constant shear rate, $\dot{\epsilon} = \alpha \times \dot{\epsilon}_0$, along the x-axis for a time duration $\Delta t \approx 0.6$ μs, with the parameter $\alpha = 1.0$, 1.5, and 2.0. The length of the simulation is chosen to be sufficiently long for the velocity center of mass of the droplet, V_{COM}, to level off to a plateau whose value matches that obtained from the stationary velocity profile of laminar flow, $V_{COM} = \dot{\epsilon} \times L_y/2$, with $L_y \approx 77$ nm, the size of the simulation box along the y-direction (*cf.* Figure 2a). The flow is then abruptly halted and the dynamical stability of the nanodroplet is studied for a time duration $\Delta t \approx 0.6$ μs.

Representative snapshots of the structural morphology of the armored nanodroplets obtained after $t \approx 0.6$ μs and $t \approx 1.2$ μs, identified in Figure 2a, are shown in Figure 2b. Visual inspection shows different morphologies depending on the intensity of the shear rate and the relaxation of the system. The changes in structural morphology are quantitatively assessed with the measure of the relative shape anisotropy parameter, κ^2, which reflects both the symmetry and dimensionality of the system[68,69] (see Methods). As shown in Figure 2a (right panel), we observe the increase of κ^2 for a relatively short time until it levels off to a plateau when the velocity profile of the laminar fluid becomes stationary, and its value depends on the intensity of the shear rate. In Figure 2b and Figure S3a in the SI, we observe the increase of κ^2, associated with the elongation of the droplet along the deformation axis x and with the squeezing of the crater-like depression along the orthogonal z-direction. ($HC1_{a,b,c}$).

When the flow is abruptly halted at $t \approx 0.6$ μs, we observe either the relaxation of κ^2 toward its initial value ($HC1_a^*$) or the formation of a long-lived anisotropic structure ($HC1_{b,c}^*$), depending on the intensity of $\dot{\epsilon}$. The specificity of the structural morphology of $HC1_{b,c}^*$ can be explained by the formation of a jammed particle layer at the droplet interface, in qualitative agreement with recently reported experimental observations.[28] To do so, we assess the characteristics of the NP interfacial layer of $HC1_{a,b,c}^*$ with the analysis of the three-phase contact angle distribution and the NP radial distribution function of small and large NPs. Within the range of shear rates considered in this work, $\theta_C^{(L)}$ follows a Gaussian distribution of mean $\mu_L \approx 87.2°$ and standard deviation $\sigma_L \approx 1.8°$, similar to the one measured in both the initial and buckled configurations (*cf.* Figure 1c). $\theta_C^{(S)}$, on the other hand, shows a skewed unimodal distribution with a central peak located at the same value as the one measured for both the initial and buckled configurations. The skewness of the distribution does not depend significantly on the intensity of the shear rate within the standard errors (*cf.* Figure S3 in the SI).

Most importantly, the radial distribution functions, g_S and g_L, of small and large NPs, respectively, show different behaviors depending on the size of the NPs, as shown in Figure 2c. Whereas g_S follows the same evolution as the one measured in HC_1 before the shear rate is applied, the evolution of g_L reflects the local reorganization of the layer made solely of large NPs at

https://doi.org/10.1021/acsnano.1c00955
ACS Nano XXXX, XXX, XXX−XXX

the droplet interface, as shown with the gradual decrease of its first peak associated with the first coordination sphere, eventually recovering the distribution observed in the initial spherical configuration shown in Figure 1d.

From the nonequilibrium simulations performed above, we showed the ability of the NP interfacial layer to control the structural evolution and dynamical stability of the armored nanodroplets under the application of external homogeneous shear flow of the surrounding fluid. Whereas the formation of the *pocket-like* structures was essentially driven by the reorganization of the small NPs at the liquid/liquid interface, the dynamical evolution under shear flow appears to be driven by steric effects with the local reorganization of the large NPs forming the jammed NP coverage at the droplet interface, which can be selectively tuned with the intensity of the shear rate. These results suggest that the morphology of the *pocket-like* armored droplet could be dynamically adjusted to accommodate probe loads of various sizes, as we investigate in the following.

Encapsulation and Release of Probe Load. Our results so far allow us to address our second aim of investigating the dynamical response of the system under shear stress, when the buckled armored nanodroplet is first loaded with a probe load, as shown in Figure 3a. We determine the ability of $HC1_c$ to lead to the encapsulation or release of the solutes under flow conditions identical to those studied in the free configuration. We consider the largest shear rate, $\dot{\epsilon} = 2 \times \dot{\epsilon}_0 \approx 1.8\ \mathrm{ns}^{-1}$, which shows the strongest morphological deformation of the system, as shown in Figure 2a (right panel). Two spherical hydrophobic solutes are considered: one small (S_S) with radius $r_S^{(s)} \approx 4$ nm and one large (S_L), with a radius $r_L^{(s)} \approx 8$ nm, respectively. The sizes of S_S and S_L are specifically chosen so that they can be initially loaded in the crater-like depression formed at the interface of HC1, obtained after the last removal of water (*cf.* Figure 1a). S_S and S_L, however, differ in their ability to eventually fit or not in $HC1_c$ when the shear stress is applied. The characteristics of the spherical solutes in the DPD framework are given in the Methods section.

The system is first stressed under constant shear rate along the x-axis for a time duration $\Delta t \approx 0.6\ \mu$s, sufficiently long to observe the flow-assisted encapsulation or release of the small and large solutes, respectively. The flow is then abruptly halted, and the relaxation of the system is studied for a time duration $\Delta t \approx 0.6\ \mu$s. In Figure 3a we show representative snapshots of the systems loaded with the two spherical solutes, S_S and S_L, at different simulation stages. When the solute is sufficiently small, the particle-laden interface folds inward under surface stress, leading to the encapsulation of the solute. When the solute is sufficiently large, however, the crater-like depression cannot accommodate the solute when the system is stressed. Therefore, S_L is progressively expelled from the pocket following the narrowing and elongation of the nanodroplet. As the flow is abruptly halted, the armored nanodroplet relaxes its structural morphology, accommodating the solute load inside the residual pocket, regardless the size of the load.

The evolution of the structural morphology of the loaded nanodroplets is quantitatively assessed with the estimation of the relative shape anisotropy, κ^2, as shown in Figure 3b. In particular, we compare the average value of κ^2 in the stationary regime, *i.e.*, $0.2\ \mu\mathrm{s} \le t \le 0.6\ \mu$s, defined as $\langle\kappa^2\rangle = \frac{1}{\Delta t}\int \kappa^2(t)\ \mathrm{d}t$, along with the relative change $\delta\kappa^2 = |\kappa^2(t = 1.2\ \mu\mathrm{s}) - \kappa^2(t = 0.6\ \mu\mathrm{s})|/\kappa^2(t = 0.6\ \mu\mathrm{s})$, measured between the beginning ($t = 0.6\ \mu$s) and the end ($t = 1.2\ \mu$s) of the relaxation period. As shown in Table 2, the values of $\langle\kappa^2\rangle$ estimated in the free and loaded configurations do not differ significantly within the standard errors, suggesting the pocket-like nanodroplet passively encapsulates or expels the small and large solutes, respectively, under the flow conditions and solute characteristics considered in this work. When the flow is abruptly halted, on the other hand, we observe the relaxation of the system, which accommodates the solute load inside the residual pockets. During this process, the relaxation of the structural morphology of the loaded nanodroplets differs from the solute-free configuration, as quantified with the relative change $\delta\kappa^2$ in Table 2, in qualitative agreement with the visual inspection in Figure 3a.

Table 2. Estimation of the Average Value of κ^2 When the System Reaches a Stationary State under Flow Conditions, $\langle\kappa^2\rangle$, and the Relative Change $\delta\kappa^2$ between the Beginning and the End of the Relaxation Period[a]

	free	S_S	S_L
$\langle\kappa^2\rangle$	0.81 ± 0.02	0.79 ± 0.04	0.80 ± 0.05
$\delta\kappa^2$	1.2 ± 0.3%	4.4 ± 1.6%	6.4 ± 4.5%

[a]Uncertainties are determined by considering three replicas of the systems and calculating the standard error.

The results above highlight the ability of the buckled armored droplets to dynamically adjust their morphology under external stress and adapt their response to probe loads with definite size and shape. This versatility is essential for the design of soft nanocarriers capable of adapting their physical properties when exposed to an external stimulus, such as mechanical stress, in complex ambients, as discussed in the next section.

Perspectives in Delivery Technology. The flow-assisted encapsulation and release of load probes in armored nanodroplets reported so far can be extended to systems of larger dimensions under conditions similar to those expected in the high-shear regime of spreading topical medication on the skin (such as creams and ointments) and the transport of targeted carriers in pathological alterations of the vascular system (such as venous or arterial thrombosis). These predictions would depend on the original dimension of the spherical droplet along with the initial NP surface coverage and the NP dimension to droplet size ratio, which would affect the surface area to volume ratio of the system and the average surface pressure of the particle-laden interface,[63] respectively.

To extend our results, the flow properties of the system are analyzed with two essential control parameters, *i.e.*, the Weber number (We) and the Ohnesorge number (Oh), commonly used in microfluidic[70,71] and droplet formation.[72] The Weber number, $We = \rho_o v^2 d_D/\gamma$, represents the ratio of the disrupting inertial force to the restorative surface tension force, where ρ_o and v are the density and the relative velocity of the ambient fluid (decane oil) and d_D and γ are the diameter and the interfacial tension of the droplet, respectively. The Ohnesorge number, $Oh = \mu_W/\sqrt{\rho_W \gamma d_D}$, represents the relative importance of the viscous force to the inertial and surface tension forces, where μ_W and ρ_W are the dynamic viscosity and the density of the water droplet, respectively. From the calculation of Oh, one can define the critical Weber number, $We_C = 12(1 + 1.5 \times Oh^{0.74})$, which corresponds to the minimum Weber

https://doi.org/10.1021/acsnano.1c00955
ACS Nano XXXX, XXX, XXX−XXX

number for a droplet to exhibit breakup modes.[73] Given $\gamma \approx 51.7$ mN·m^{-1} is the interfacial tension for a planar decane/water interface,[46,56] $\rho_W \approx 1000$ kg·m^{-3} and $\rho_o \approx 726$ kg·m^{-3} are the density of water and decane oil, respectively, $v \approx 50-70$ m·s^{-1} is the stationary velocity of the laminar flow (*cf.* Figure 3a), $\mu_W = 8.9 \times 10^{-4}$ Pa·s is the dynamic viscosity of water, and $d_D \approx 40$ nm is the droplet diameter obtained from the measure of R_{GYR} (*cf.* Figure 2a), we obtain $Oh \approx 0.6$, $We_C \approx 25$, and $We \approx 1.4-2.8$, indicating the armored droplets considered in the flow-assisted encapsulation and release processes are outside their breakup regime.[74]

Now, based on the estimation of the Weber number, we extend our predictions to the high-shear regime of spreading water-in-oil/oil-in-water emulsion-based products. Given the relation $v \approx \dot{\epsilon} \times L_\perp$ with $L_\perp$ being the dimension of the system orthogonal to the flow direction, we obtain $We \approx \rho_o \dot{\epsilon}^2 L_\perp^2 d_D/\gamma$. Considering the average thickness of a cream $L_\perp \approx 1$ cm and representative shear rates $\dot{\epsilon} \approx 10^2-10^3$ s^{-1},[75,76] we obtain the characteristic dimension of the emulsion droplet $d_D \approx 1-100$ μm, corresponding to the minimal droplet size to observe the encapsulation or release mechanism, in agreement with the range of characteristic droplet sizes commonly used in topical pharmaceutical products.[76,77]

Either by skin adsorption or other intake paths, targeted carriers can reach the bloodstream as required. The complexity of the flow scenarios present in the circulatory system defies the full description of the behavior of our model carrier once entering the body. However, it is possible to put our predictions into perspective with the transport of our model carrier in the vascular subsystem, in particular in the pathological flow conditions encountered in venous or arterial thrombosis.[78] The fluid properties of the hepatic artery (representative of a large artery) in nonpathological conditions have a characteristic dimension $L_\perp \approx 5$ mm and shear rate $\dot{\epsilon} \approx 500$ s^{-1}.[79] A pathological flow, on the other hand, can be defined as where the blood reaches shear rates $\dot{\epsilon} > 5000$ s^{-1}, resulting, for example, from pathological clotting of blood within the lumen of a vessel.[80] Considering $\rho_{blood} \approx 1060$ kg·m^{-3} and $\gamma \approx 42$ mN·m^{-1} as representative values of the average density and interfacial tension (against fluorocarbon) of the blood fluid,[81] along with the narrowing of the pathological vessel, $L_\perp \rightarrow L_\perp/2$, we obtain $d_D \approx 500$ nm for the minimal droplet dimension under the condition of a hepatic artery with pathological alterations to observe the encapsulation or release mechanism. For comparison, we obtain $d_D \approx 10$ μm for the minimal droplet dimension in the conditions of the normal hepatic artery, in the range of sizes characteristic of leucocytes and red blood cells.[82]

This analysis suggests that the process of targeted delivery of active compounds (such as antithrombotic agents) can be selectively controlled with the size of the model nanocarrier, as shown in Figure 4, depending on the dimension of the compound. For instance, cargo nanodroplets of dimension ~500 nm would only release the therapeutic payloads they carry once they reach pathological alterations where the diameter of the artery significantly decreases, increasing, consequently, the shear rate of the surrounding fluid. Finally, the important advances in the development of microfluidics devices to closely reproduce cardiovascular systemic conditions in the presence of cells and tissues[47−49] depict a framework adequate to test and refine our predictions.

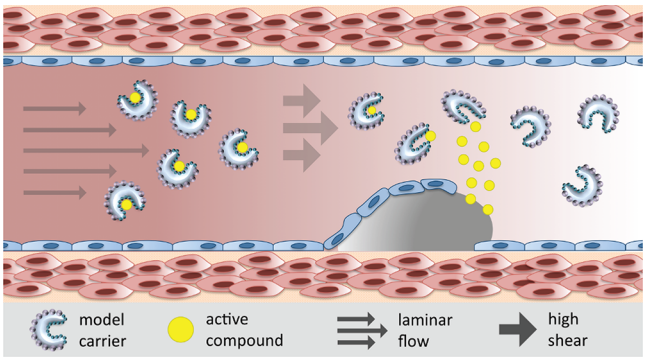

Figure 4. Perspective in delivery technology. Schematic representation of the potential application of the model nanocarrier in the high-shear regime encountered in hepatic artery thrombosis. In that scenario, the decrease in the channel diameter increases the shear rate, promoting the release of the compound (yellow). The cross-sectional view of the model nanocarrier is shown for convenience.

CONCLUSIONS

The numerical simulations discussed above allowed us to explore the design and dynamical stability of a distinctive class of soft nanocarriers inspired by Pickering nanoemulsions, which can have potential in targeted-oriented active molecule encapsulation and release under specific flow conditions. The success in controlling the creation of crater-like depressions on the surface of Pickering micron-sized droplets recently reported by Rozynek *et al.*[26] demonstrates the plausibility of our predictions as well as the dynamics here presented. The interplay between the evolution of the structural morphology of the armored nanodroplets and the organization of the NP interfacial network, when the volume of the system is reduced, is in qualitative agreement with experimental observation.[62] We showed that finite-size NPs can strongly affect the droplet shape with the formation of *pocket-like* depressions, which can structurally favor the loading of a probe load.

We then focused our analysis on the dynamical tuning of the NP distribution at the surface of the armored nanodroplets under external shear stress, which is more representative of biological ambients. The dynamical response of specifically designed *pocket-like* nanodroplets under different shear flow conditions exhibited the formation of long-lived anisotropic structures, characteristic of a jammed particle coverage at the liquid−liquid interface, associated with the dynamical rearrangement of the NP interfacial network. Most importantly, the ability of *pocket-like* nanodroplets to encapsulate or release spherical solute loads located inside the crater-like depression, during their transport under shear-flow conditions, was validated.

Our predictions on the flow-assisted encapsulation and release of load probes in armored nanodroplets were extended to systems in the micron scale encountered in pharmaceutical and cosmetic technologies. Noticeably, we demonstrated that the mechanism reported in our work could be at play at larger scales, such as those encountered in the high-shear regime of spreading creams and ointments on the skin and the transport of targeted carriers in pathological alterations of the vascular system. As an example, we put the physical properties of our model carrier into perspective within the conditions encountered in pathologies of the hepatic artery, where the formation of a blood clot inside the blood vessel can obstruct the flow of

https://doi.org/10.1021/acsnano.1c00955
ACS Nano XXXX, XXX, XXX−XXX

blood through the circulatory system, increasing the hemodynamic shear stress and the risk of bleeding complications. In particular, hepatic artery thrombosis can be a very serious complication of liver transplantation, with mortality in children as high as 70%.[83] Hence, it is essential to develop distinctive means to control the process of targeted delivery of antithrombotic agents in the vascular system.

The physical insights discussed here provide a deeper understanding on the potential role played by nanoparticle-stabilized emulsions in the biomimetic design of hybrid soft materials for targeted-oriented active load delivery. This information could be useful for a variety of applications including the design of pharmaceutical carriers for drug delivery and pathogen encapsulation, where knowledge of the rheological properties of the system must be quantitatively assessed. Eventually, our method would allow including specific interactions inside the formed cavity in order to mimic, for example, protein binding pockets or catalytic nanosurfaces. Finer morphological changes and functionalization of the surface of the armored droplets could also be considered using pH- or electro-reponsive NPs, therefore controlling their distribution and physicochemical properties at the liquid/liquid interface with external stimuli.[20−25]

METHODS

Mesoscopic Framework. The dissipative particle dynamics simulation method[84] is implemented within the simulation package LAMMPS.[85] In the DPD simulations, a particle represents a cluster of atoms rather than an individual atom. These particles interact with each other through soft particle−particle interactions. The movement of the particle can be realized by solving the Newton equation of motion:

$$\frac{d\mathbf{r}_i}{dt} = \mathbf{v}_i, \qquad m_i\frac{d\mathbf{v}_i}{dt} = \mathbf{F}_i \tag{1}$$

where m_i, $\mathbf{r}_i$, $\mathbf{v}_i$, and $\mathbf{F}_i$ denote the mass, position, velocity, and total force acting on the ith particle, respectively. The total force $\mathbf{F}_i$ is divided into three parts, the conservative force ($\mathbf{F}_{ij}^{C}$), dissipative force ($\mathbf{F}_{ij}^{D}$), and random force ($\mathbf{F}_{ij}^{R}$), and defined as $\mathbf{F}_i = \sum_{j\neq i}(\mathbf{F}_{ij}^{C} + \mathbf{F}_{ij}^{C} + \mathbf{F}_{ij}^{C})$ with

$$\mathbf{F}_{ij}^{C} = a_{ij}\sqrt{\omega(r_{ij})}\,\hat{\mathbf{r}}_{ij} \tag{2}$$

$$\mathbf{F}_{ij}^{D} = -\Gamma\omega(r_{ij})(\hat{\mathbf{r}}_{ij}\cdot\mathbf{v}_{ij})\hat{\mathbf{r}}_{ij} \tag{3}$$

$$\mathbf{F}_{ij}^{R} = \sigma\sqrt{\omega(r_{ij})}\,\theta_{ij}\hat{\mathbf{r}}_{ij} \tag{4}$$

where $\mathbf{r}_{ij} = \mathbf{r}_i - \mathbf{r}_j$, $r_{ij} = |\mathbf{r}_{ij}|$, $\hat{r}_{ij} = \mathbf{r}_{ij}/r_{ij}$, and $\mathbf{v}_{ij} = \mathbf{v}_i - \mathbf{v}_j$. The weight function $\omega(r_{ij})$ equals $(1 - r_{ij}/R_c)^2$ with a cutoff distance R_c. a_{ij}, Γ, σ, and θ_{ij} are the repulsive parameter, friction coefficient, noise amplitude, and Gaussian random variable, respectively. To keep the temperature of the system constant, Γ and σ satisfy the fluctuation−dissipation theorem as $\sigma^2 = 2\Gamma k_B T$, where k_B and T are the Boltzmann and the absolute temperature, respectively.

The system simulated here is composed of water, oil (decane), NPs, and solute molecules. Following previous work,[38,44,46,54] we choose the degree of coarse graining $N_m = 5$ with the understanding that one "water bead" (w) represents five water molecules. Within this assumption, the volume of each bead is $V_{bead} \approx 150$ Å^3. The scaled density is set to $\rho = 3$ beads/R_c^3, where R_c is the DPD cutoff distance given as $R_c = \sqrt[3]{\rho V_{bead}} \approx 0.766$ nm. The scaled mass of each bead (oil, water, solute molecule, and NP beads) was set to 1. One decane molecule is modeled as two "oil beads" (o) connected by one harmonic spring of length $0.72R_c$ and spring constant 350 k_BT/R_c.[86] The size of the triclinic simulation box (initially orthogonal) is $L_x \times L_y \times L_z \equiv 200 \times 100 \times 100\ R_c^3$, where L_x (respectively L_y and L_z) is the box length along the X (respectively Y and Z) direction. Periodic boundary conditions are applied in all three directions. The solute molecules and the NPs are modeled as hollow rigid spheres, as already described in previous work.[38,44,46,54] The hydrophobic solute molecules are made of nonpolar DPD beads, whereas the NPs contain polar (p) and nonpolar (ap) DPD beads on their surface.[87] One DPD bead was placed at the NP and solute molecule centers for convenience, as described elsewhere.[54,88] All types of beads in our simulations have a reduced mass of 1. We maintain the surface bead density on the NPs and solute molecule sufficiently high to prevent other DPD beads (either decane or water) from penetrating the NPs and solute molecules.[88]

The interaction parameters shown in Table 3 are used here. These parameters are adjusted to reproduce selected atomistic simulation results, as explained in prior work.[54] The interaction parameters between NP polar and nonpolar beads, as well as solute molecule beads, are adjusted to ensure that NPs/NPs and NPs/solute are able to assemble and disassemble without yielding permanent dimers at the water/oil interface.[54] The scaled temperature was set to 1, equivalent to 298.73 K. The time step $\delta t = 0.03 \times \tau$ was used to integrate the equations of motion, where τ is the DPD time constant. As demonstrated by Groot and Rabone,[86] the time constant of the simulation can be gauged by matching the simulated self-diffusion of water, D_{sim}, with the experimental water self-diffusion coefficient, $D_{water} = 2.43 \times 10^{-5}$ cm^2/s,[89] calculated as $\tau = \frac{N_m D_{sim} R_c^2}{D_{water}}$, as shown in previous work.[54] When $a_{w-w} = 131.5\ k_BT/R_c$, this results in a time step $\delta t = 5.6$ ps.

Table 3. DPD Interaction Parameters Expressed in k_BT/R_c Units[a]

	w	o	ap	p	s
w	131.5	198.5	178.5	110	670
o		131.5	161.5	218.5	161.5
ap			450	670	450
p				450	670
s					131.5

[a]Symbols w, o, ap, p, and s stand for water beads, oil beads, NP nonpolar beads, NP polar beads, and solute beads, respectively.

While the DPD framework satisfies the Navier−Stokes equations in the continuum limit,[84] the traditional DPD algorithm cannot reproduce the vapor−liquid coexistence of water at the droplet interface.[90] This is due to the DPD conservative force, which determines the thermodynamics of the DPD system and yields the equation of state[84]

$$p = \rho k_B T + \alpha a \rho^2 \tag{5}$$

where p is the pressure, ρ is the number density of the DPD beads, a is the repulsion strength, and α is a fitting parameter equal to 0.101 ± 0.001 in DPD reduced units.[84] As shown by Warren,[90] the DPD system is unstable for $a < 0$, so one is restricted to $a \geq 0$ and therefore to strictly repulsive (conservative) interactions. This implies that calculations such as the vapor−liquid coexistence and free-surface simulations cannot be attempted. This can be adjusted by considering higher order terms of the density, ρ, in eq 5, *i.e.*, making the conservative force in eq 2 density dependent.[90]

Nonequilibrium Simulation. To simulate the response of the system subjected to a homogeneous shear flow, we employ the SLLOD algorithm[65,66] coupled with the Lee−Edwards periodic boundary conditions,[67] as implemented in the simulation package LAMMPS.[85] The SLLOD algorithm modifies the equations of motion in eq 1 as

$$\frac{d\mathbf{r}_i}{dt} = \mathbf{v}_i + \mathbf{e}_x\dot{\epsilon}r_{i,y} \tag{6}$$

https://doi.org/10.1021/acsnano.1c00955
ACS Nano XXXX, XXX, XXX−XXX

$$m_i \frac{d\mathbf{v}_i}{dt} = \mathbf{F}_i - m_i \mathbf{e}_x \dot{\epsilon} v_{i,y} \tag{7}$$

where $\dot{\epsilon} = \partial v_x/\partial r_y$ is the shear rate of the external flow and $\mathbf{e}_{x,y}$ are the unit vectors along the x and y directions, respectively. The velocity of the ith particle is divided into two parts, that is, the peculiar velocity $\mathbf{v}_i$ representing the random thermal motions and the shear flow velocity $\mathbf{e}_x \dot{\epsilon} v_{i,y}$ relating to the external disturbance strength. Specifically, we impose a linear velocity profile in the x direction with a constant gradient in the y direction, keeping the density of the system constant, by changing the xy-tilt factor, T_{xy}, of the triclinic simulation box at a constant shear rate, $\dot{\epsilon}$, as

$$T_{xy}(t) = T_{xy}^{(0)} + \dot{\epsilon} L_0 \Delta t \tag{8}$$

In eq 8, $T_{xy}^{(0)}$ and L_0 are the initial tilt factor and the original length of the box perpendicular to the shear direction. This can be related to the shear stress of the external shear flow $\tau_s = \mu\dot{\epsilon}$, with μ being the dynamic viscosity of the continuous phase.

Three-Phase Contact Angle. To estimate the three-phase contact angle, θ_C, for the NPs on the droplets, we calculate the fraction of the spherical NP surface area that is wetted by water,[91]

$$\theta_C = 180 - \arccos\left(1 - \frac{2A_w}{4\pi R^2}\right) \tag{9}$$

where A_w is the area of the NP surface that is wetted by water and R is the radius of the NP. The ratio $A_w/4\pi R^2$ is obtained by dividing the number of NP surface beads (ap or p) that are wetted by water by the total number of beads on the NP surface. One surface bead is wet by water if a water bead is the solvent bead nearest to it. One standard deviation from the average is used to estimate the statistical uncertainty.

Interfacial Tension. The interfacial tension γ at the water/oil interface as a function of the NP surface coverage Φ is calculated as[54,56]

$$\gamma = \left\langle P_{zz} - \frac{P_{xx} + P_{yy}}{2} \right\rangle \frac{L_z}{2} \tag{10}$$

In eq 10, P_{ij} is the ij element of the pressure tensor, L_z is the simulation box length in the z dimension, and the angular brackets denote the ensemble average.

Self-Diffusion Coefficient. To characterize the self-diffusion coefficient of the NPs at the water/oil interface, we estimate the mean squared displacement of a single NP adsorbed at a planar interface parallel to the $x-y$ plane. For each particle size, the simulated diffusion coefficient is estimated according to

$$D_{x-y} = \frac{1}{4} \left\langle \frac{|r_i(t) - r_i(0)|^2}{t} \right\rangle \tag{11}$$

where $r_i(t)$ is the position of particle i at time t on the plane of the interface.

Gyration Tensor. To measure the evolution of the structural morphology of the emulsion droplet, we estimate the principal components of the gyration tensor,[38,68,92] which allow the evaluation of the overall shape of the system and reveal its symmetry. Considering the definition for the gyration tensor,

$$\mathcal{T}_{GYR} = \frac{1}{N} \begin{bmatrix} \sum x_i^2 & \sum x_i y_i & \sum x_i z_i \\ \sum x_i y_i & \sum y_i^2 & \sum y_i z_i \\ \sum x_i z_i & \sum y_i z_i & \sum z_i^2 \end{bmatrix} \tag{12}$$

where the summation is performed over N atoms and the coordinates x, y, and z are related to the geometrical center of the atoms, one can define a reference frame where $\mathcal{T}_{GYR}$ can be diagonalized:

$$\mathcal{T}_{GYR}^{diag} = \begin{bmatrix} S_1^2 & 0 & 0 \\ 0 & S_2^2 & 0 \\ 0 & 0 & S_3^2 \end{bmatrix} \tag{13}$$

In eq 13, we follow the convention of indexing the eigenvalues according to their magnitude, *i.e.*, $S_1^2 > S_2^2 > S_3^2$. We define the radius of gyration $R_{GYR}^2 \equiv S_1^2 + S_2^2 + S_3^2$ and the relative shape anisotropy $\kappa^2 = \frac{3}{2}\frac{S_1^4 + S_2^4 + S_3^4}{(S_1^2 + S_2^2 + S_3^2)^2} - \frac{1}{2}$, and we calculate R_{GYR} and κ^2 using the centers of the water beads.

ASSOCIATED CONTENT

Supporting Information

The Supporting Information is available free of charge at https://pubs.acs.org/doi/10.1021/acsnano.1c00955.

Additional information about numerical simulation methods; system characterization (PDF)

AUTHOR INFORMATION

Corresponding Author

François Sicard − *Department of Physics and Astronomy, University College London, WC1E 6BT London, U.K.; Department of Chemical Engineering, University College London, WC1E 7JE London, U.K.;* orcid.org/0000-0003-1408-7963; Email: francois.sicard@free.fr

Author

Jhoan Toro-Mendoza − *Centro de Estudios Interdisciplinarios de la Fisica, Instituto Venezolano de Investigaciones Cientificas, Caracas 1020A, Venezuela;* orcid.org/0000-0003-4916-7445

Complete contact information is available at: https://pubs.acs.org/10.1021/acsnano.1c00955

Notes

The authors declare no competing financial interest.

ACKNOWLEDGMENTS

F.S. acknowledges Javier Reguera for fruitful suggestions and Alberto Striolo for useful discussions. The authors thank the anonymous reviewers for their many insightful comments and suggestions and Reginald Hardman for careful reading of the manuscript. *Via* our membership of the UKs HEC Materials Chemistry Consortium, which is funded by EPSRC (EP/L000202), this work used the ARCHER UK National Supercomputing Service (http://www.archer.ac.uk).

REFERENCES

(1) Genchi, G. G.; Marino, A.; Tapeinos, C.; Ciofani, G. Smart Materials Meet Multifunctional Biomedical Devices: Current and Prospective Implications for Nanomedicine. *Front. Bioeng. Biotechnol.* **2017**, *5*, 80.

(2) Wang, P., Ed. *Smart Materials for Advanced Environmental Applications*; Smart Materials Series; The Royal Society of Chemistry: Cambridge, UK, 2016; pp P001−252.

(3) Shi, S.; Russell, T. Nanoparticle Assembly at Liquid−Liquid Interfaces: From the Nanoscale to Mesoscale. *Adv. Mater.* **2018**, *30*, 1−22.

(4) Hu, C.; Pané, S.; Nelson, B. Soft Micro- and Nanorobotics. *Annual Review of Control, Robotics, and Autonomous Systems* **2018**, *1*, 53−75.

(5) Jani, J. M.; Leary, M.; Subic, A.; Gibson, M. A Review of Shape Memory Alloy Research, Applications and Opportunities. *Mater. Eng.* **2014**, *56*, 1078−113.
(6) Geryak, R.; Tsukruk, V. V. Reconfigurable and Actuating Structures from Soft Materials. *Soft Matter* **2014**, *10*, 1246−63.
(7) Addinall, R.; Ackermann, T.; Kolaric, I. *Nanostructured Materials for Soft Robotics−Sensors and Actuators. Soft Robotics*; Springer: Heidelberg, Berlin, 2015; pp 147−156.
(8) Pickering, S. CXCVI.-Emulsions. *J. Chem. Soc., Trans.* **1907**, *91*, 2001−2021.
(9) Yang, H.; Fu, L.; Wei, L.; Liang, J.; Binks, B. Compartmentalization of Incompatible Reagents within Pickering Emulsion Droplets for One-Pot Cascade Reactions. *J. Am. Chem. Soc.* **2015**, *137*, 1362−1371.
(10) Rozynek, Z.; Bielas, R.; Jozefczak, A. Efficient Formation of Oil-in-Oil Pickering Emulsions with Narrow Size Distributions by Using Electric Fields. *Soft Matter* **2018**, *14*, 5140.
(11) Garbin, V. Collapse Mechanisms and Extreme Deformation of Particle-Laden Interfaces. *Curr. Opin. Colloid Interface Sci.* **2019**, *39*, 202−211.
(12) Rozynek, Z.; Banaszak, J.; Mikkelsen, A.; Khobaib, K.; Magdziarz, A. Electrorotation of Particle-Coated Droplets: From Fundamentals to Applications. *Soft Matter* **2021**, *17*, 4413−4425.
(13) Toro-Mendoza, J.; Rodriguez-Lopez, G.; Paredes-Altuve, O. Brownian Diffusion of a Particle at an Air/Liquid Interface: The Elastic (Not Viscous) Response of the Surface. *Phys. Chem. Chem. Phys.* **2017**, *19*, 9092−9095.
(14) Silva, H.; Cerqueira, M.; Vicente, A. Nanoemulsions for Food Applications: Development and Characterization. *Food Bioprocess Technol.* **2012**, *5*, 854−867.
(15) Rosenblum, D.; Joshi, N.; Tao, W.; Karp, J.; Peer, D. Progress and Challenges towards Targeted Delivery of Cancer Therapeutics. *Nat. Commun.* **2018**, *9*, 1410.
(16) Aziz, Z.; Mohd-Nasir, H.; Ahmad, A.; Setapar, S.; Peng, W.; Chuo, S.; Khatoon, A.; Umar, K.; Yaqoob, A.; Ibrahim, M. Role of Nanotechnology for Design and Development of Cosmeceutical: Application in Makeup and Skin Care. *Front. Chem.* **2019**, *7*, 739.
(17) Kowalczyk, B.; Lagzi, I.; Grzybowski, B. "Nanoarmoured" Droplets of Different Shapes Formed by Interfacial Self-Assembly and Cross Linking of Metal Nanoparticles. *Nanoscale* **2010**, *2*, 2366−2369.
(18) Stephenson, G.; Parker, R.; Lan, Y.; Yu, Z.; Scherman, O.; Abel, C. Supramolecular Colloidosomes: Fabrication, Characterisation and Triggered Release of Cargo. *Chem. Commun.* **2014**, *50*, 7048.
(19) Melle, S.; Lask, M.; Fuller, G. Pickering Emulsions with Controllable Stability. *Langmuir* **2005**, *21*, 2158−2162.
(20) Dommersnes, P.; Rozynek, Z.; Mikkelsen, A.; Castberg, R.; Kjerstad, K.; Hersvik, K.; Fossum, J. Active Structuring of Colloidal Armour on Liquid Drops. *Nat. Commun.* **2013**, *4*, 2066.
(21) Rozynek, Z.; Dommersnes, P.; Mikkelsen, A.; Michels, L.; Fossum, J. Electrohydrodynamic Controlled Assembly and Fracturing of Thin Colloidal Particle Films Confined at Drop Interfaces. *Eur. Phys. J.: Spec. Top.* **2014**, *223*, 1859−1867.
(22) Mikkelsen, A.; Wojciechowski, J.; Rajnak, M.; Kurimsky, J.; Khobaib, K.; Kertmen, A.; Rozynek, Z. Electric Field-Driven Assembly of Sulfonated Polystyrene Microspheres. *Materials* **2017**, *10*, 329.
(23) Mikkelsen, A.; Khobaib, K.; Eriksen, F.; Maloy, K.; Rozynek, Z. Particle-Covered Drops in Electric Fields: Drop Deformation and Surface Particle Organization. *Soft Matter* **2018**, *14*, 5442.
(24) Rozynek, Z.; Khobaib, K.; Mikkelsen, A. Opening and Closing of Particle Shells on Droplets *via* Electric Fields and Its Applications. *ACS Appl. Mater. Interfaces* **2019**, *11*, 22840−22850.
(25) Mikkelsen, A.; Rozynek, Z. Mechanical Properties of Particle Films on Curved Interfaces Probed through Electric Field-Induced Wrinkling of Particle Shells. *ACS Appl. Mater. Interfaces* **2019**, *11*, 29296−29407.
(26) Khobaib, K.; Mikkelsen, A.; Vincent-Dospital, T.; Rozynek, Z. Electric-field-induced Deformation, Yielding, and Crumpling of Jammed Particle Shells Formed on Non-Spherical Pickering Droplets. *Soft Matter* **2021**, *17*, 5006.
(27) Ortiz, D. G.; Pochat-Bohatier, C.; Cambedouzou, J.; Bechelany, M.; Miele, P. Current Trends in Pickering Emulsions: Particle Morphology and Applications. *Engineering* **2020**, *6*, 468−482.
(28) Kaganyuk, M.; Mohraz, A. Shear-Induced Deformation and Interfacial Jamming of Solid-Stabilized Droplets. *Soft Matter* **2020**, *16*, 4431.
(29) Frelichowska, J.; Bolzinger, M.-A.; Valour, J.-P.; Mouaziz, H.; Pelletier, J.; Chevalier, Y. Pickering W/O Emulsions: Drug Release and Topical Delivery. *Int. J. Pharm.* **2009**, *23*, 7−15.
(30) Aparicio, R.; García-Celma, M.; Vinardell, M. P.; Mitjans, M. *In Vitro* Studies of the Hemolytic Activity of Microemulsions in Human Erythrocytes. *J. Pharm. Biomed. Anal.* **2005**, *39*, 1063−7.
(31) Chevalier, Y.; Bolzinger, M. Emulsions Stabilized with Solid Nanoparticles: Pickering Emulsions. *Colloids Surf., A* **2013**, *439*, 23−34.
(32) Yang, H.; Fu, L.; Wei, L.; Liang, J.; Binks, B. Compartmentalization of Incompatible Reagents within Pickering Emulsion Droplets for One-Pot Cascade Reactions. *J. Am. Chem. Soc.* **2015**, *137*, 1362−1371.
(33) Shi, D.; Faria, J.; Pham, T.; Resasco, D. Enhanced Activity and Selectivity of Fischer−Tropsch Synthesis Catalysts in Water/Oil Emulsions. *ACS Catal.* **2014**, *4*, 1944−1952.
(34) Faria, J.; Ruiz, M. P.; Resasco, D. Carbon Nanotube/Zeolite Hybrid Catalysts for Glucose Conversion in Water/Oil Emulsions. *ACS Catal.* **2015**, *5*, 4761−4771.
(35) Qu, Y.; Huang, R.; Qi, W.; Qu, Q.; Su, R.; He, Z. Structural Insight into Stabilization of Pickering Emulsions with Fe3O4@SiO2 Nanoparticles for Enzyme Catalysis in Organic Media. *Part. Part. Syst. Charact.* **2017**, *34*, 1700117.
(36) Shen, X.; Bonde, J. S.; Kamra, T.; Bülow, L.; Leo, J.; Linke, D.; Ye, L. Bacterial Imprinting at Pickering Emulsion Interfaces. *Angew. Chem., Int. Ed.* **2014**, *53*, 10687−10690.
(37) Horváth, B.; Balázs, V.; Varga, A.; Böszörményi, A.; Kocsis, B.; Horváth, G.; Széchenyi, A. Preparation, Characterisation and Microbiological Examination of Pickering Nano-Emulsions Containing Essential Oils, and Their Effect on Streptococcus Mutans Biofilm Treatment. *Sci. Rep.* **2019**, *9*, 16611.
(38) Sicard, F.; Striolo, A. Numerical Analysis of Pickering Emulsion Stability: Insights from ABMD Simulations. *Faraday Discuss.* **2016**, *191*, 287−304.
(39) Seemann, R.; Brinkmann, M.; Pfohl, T.; Herminghaus, S. Droplet Based Microfluidics. *Rep. Prog. Phys.* **2012**, *75*, 16601−2012.
(40) Orellana, L. C.; Baret, J. Rapid Stabilization of Droplets by Particles in Microfluidics: Role of Droplet Formation. *Chem. System Chem.* **2019**, *1*, 16−24.
(41) Reguera, J.; Ponomarev, E.; Geue, T.; Stellacci, F.; Bresme, F.; Moglianetti, M. Contact Angle and Adsorption Energies of Nanoparticles at the Air-Liquid Interface Determined by Neutron Reflectivity and Molecular Dynamics. *Nanoscale* **2012**, *7*, 5665−5673.
(42) Giner-Casares, J.; Reguera, J. Directed Self-Assembly of Inorganic Nanoparticles at Air/Liquid Interfaces. *Nanoscale* **2016**, *8*, 16589−16595.
(43) Binks, B.; Yin, D. Pickering Emulsions Stabilized by Hydrophilic Nanoparticles: *In Situ* Surface Modification by Oil. *Soft Matter* **2016**, *12*, 6858−6867.
(44) Sicard, F.; Striolo, A. Buckling in Armored Droplet. *Nanoscale* **2017**, *9*, 8567−8572.
(45) Sicard, F.; Striolo, A. In *Anisotropic Particle Assemblies*; Wu, N., Lee, D., Striolo, A., Eds.; Elsevier: Amsterdam, 2018; pp 167−200.
(46) Sicard, F.; Toro-Mendoza, J.; Striolo, A. Nanoparticles Actively Fragment Armored Droplets. *ACS Nano* **2019**, *13*, 9498−9503.
(47) Ma, Q.; Ma, H.; Xu, F.; Wang, X.; Sun, W. Microfluidics in Cardiovascular Disease Research: State of the Art and Future Outlook. *Microsystems & Nanoengineering* **2021**, *7*, 1−19.
(48) Zhang, L.; Chen, Q.; Ma, Y.; Sun, J. Microfluidic Methods for Fabrication and Engineering of Nanoparticle Drug Delivery Systems. *ACS Applied Bio Materials* **2020**, *3*, 107−120.

https://doi.org/10.1021/acsnano.1c00955
ACS Nano XXXX, XXX, XXX−XXX

(49) Rabiee, N.; Ahmadi, S.; Fatahi, Y.; Rabiee, M.; Bagherzadeh, M.; Dinarvand, R.; Bagheri, B.; Zarrintaj, P.; Saeb, M. R.; Webster, T. J. Nanotechnology-Assisted Microfluidic Systems: From Bench to Bedside. *Nanomedicine* **2021**, *16*, 237−258.
(50) Groot, R.; Warren, P. Dissipative Particle Dynamics: Bridging the Gap between Atomistic and Mesoscopic Simulation. *J. Chem. Phys.* **1997**, *107*, 4423−4435.
(51) Zhang, J.; Grzybowski, B.; Granick, S. Janus Particle Synthesis, Assembly, and Application. *Langmuir* **2017**, *33*, 6964−6977.
(52) Agrawal, G.; Agrawal, R. Janus Nanoparticles: Recent Advances in Their Interfacial and Biomedical Applications. *ACS Appl. Nano Mater.* **2019**, *2*, 1738−1757.
(53) Binks, B.; Lumsdon, S. Influence of Particle Wettability on the Type and Stability of Surfactant-Free Emulsions. *Langmuir* **2000**, *16*, 8622−8631.
(54) Luu, X.-C.; Yu, J.; Striolo, A. Nanoparticles Adsorbed at the Water/Oil Interface: Coverage and Composition Effects on Structure and Diffusion. *Langmuir* **2013**, *29*, 7221.
(55) Fan, H.; Resasco, D.; Striolo, A. Amphiphilic Silica Nanoparticles at the Decane-Water Interface: Insights from Atomistic Simulations. *Langmuir* **2011**, *27*, 5264−5274.
(56) Fan, H.; Striolo, A. Nanoparticle Effects on the Water-Oil Interfacial Tension. *Phys. Rev. E* **2012**, *86*, 051610.
(57) Arnaudov, L.; Cayre, O.; Cohen Stuart, M.; Stoyanov, S.; Paunov, V. Measuring the Three-Phase Contact Angle of Nanoparticles at Fluid Interfaces. *Phys. Chem. Chem. Phys.* **2010**, *12*, 328−331.
(58) Binks, B.; Fletcher, P. Pickering Emulsions Stabilized by Monodisperse Latex Particles: Effects of Particle Size. *Langmuir* **2001**, *16*, 21−41.
(59) Jiang, S.; Granick, S. Janus Balance of Amphiphilic Colloidal Particles. *J. Chem. Phys.* **2007**, *127*, 161102.
(60) Khedr, A.; Striolo, A. Self-Assembly of Mono- and Poly-Dispersed Nanoparticles on Emulsion Droplets: Antagonistic *vs.* Synergistic Effects as a Function of Particle Size. *Phys. Chem. Chem. Phys.* **2020**, *22*, 22662.
(61) Wang, D.; Yordanov, S.; Paroor, H.; Mukhopadhyay, A.; Li, C.; Butt, H.; Koynov, K. Probing Diffusion of Single Nanoparticles at Water−Oil Interfaces. *Small* **2011**, *7*, 3502−3507.
(62) Datta, S.; Shum, H.; Weitz, D. Controlled Buckling and Crumpling of Nanoparticle-Coated Droplets. *Langmuir* **2010**, *26*, 18612−18616.
(63) Gu, C.; Botto, L. Buckling *vs.* Particle Desorption in a Particle-Covered Drop Subject to Compressive Surface Stresses: A Simulation Study. *Soft Matter* **2018**, *14*, 711.
(64) Basavaraj, M.; Fuller, G.; Fransaer, J.; Vermant, J. Packing, Flipping, and Buckling Transitions in Compressed Monolayers of Ellipsoidal Latex Particles. *Langmuir* **2006**, *22*, 6605−6612.
(65) Evans, D. J.; Morriss, G. P. Non-Newtonian Molecular Dynamics. *Comput. Phys. Rep.* **1984**, *1*, 297.
(66) Evans, D.; Morriss, G. Nonlinear-Response Theory for Steady Planar Couette Flow. *Phys. Rev. A: At., Mol., Opt. Phys.* **1984**, *30*, 1528.
(67) Lees, A.; Edwards, S. F. The Computer Study of Transport Processes under Extreme Conditions. *J. Phys. C: Solid State Phys.* **1972**, *5*, 1921.
(68) Vymetal, J.; Vondrásek, J. Gyration- and Inertia-Tensor-Based Collective Coordinates for Metadynamics. Application on the Conformational Behavior of Polyalanine Peptides and Trp-Cage Folding. *J. Phys. Chem. A* **2011**, *115*, 11455−11465.
(69) Arkin, H.; Janke, W. Gyration Tensor Based Analysis of the Shapes of Polymer Chains in an Attractive Spherical Cage. *J. Chem. Phys.* **2013**, *138*, 054904.
(70) Hall, S.; Pacek, A.; Kowalski, A.; Cooke, M.; Rothman, D. The Effect of Scale and Interfacial Tension on Liquid−Liquid Dispersion in In-Line Silverson Rotor−Stator Mixers. *Chem. Eng. Res. Des.* **2013**, *91*, 2156−2168.
(71) Xu, Z.; Wang, T.; Che, Z. Droplet Deformation and Breakup in Shear Flow of Air. *Phys. Fluids* **2020**, *32*, 052109.
(72) Roas-Escalona, N.; Williams, Y. O.; Cruz-Barrios, E.; Toro-Mendoza, J. Intertwining Roles of the Disperse Phase Properties during Emulsification. *Langmuir* **2018**, *34*, 6480−6488.
(73) Gelfand, B. Droplet Breakup Phenomena in Flows with Velocity Lag. *Prog. Energy Combust. Sci.* **1996**, *22*, 201−265.
(74) Derby, B. Inkjet Printing of Functional and Structural Materials: Fluid Property Requirements, Feature Stability, and Resolution. *Annu. Rev. Mater. Res.* **2010**, *40*, 395−414.
(75) Walicka, A.; Falicki, J.; Iwanowska-Chomiak, B. Rheology of Drugs for Topical and Transdermal Delivery. *Int. J. of Applied Mechanics and Engineering* **2019**, *24*, 179−198.
(76) Simoes, A.; Veiga, F.; Vitorino, C. Progressing towards the Sustainable Development of Cream Formulations. *Pharmaceutics* **2020**, *12*, 647.
(77) Lu, G.; Gao, P. In *Handbook of Non-Invasive Drug Delivery Systems*; Kulkarni, V. S., Ed.; Personal Care & Cosmetic Technology; William Andrew Publishing: Boston, USA, 2010; pp 59−94.
(78) Esmon, C. Basic Mechanisms and Pathogenesis of Venous Thrombosis. *Blood Rev.* **2009**, *23*, 225−229.
(79) Sakariassen, K.; Orning, L.; Turitto, V. The Impact of Blood Shear Rate on Arterial Thrombus Formation. *Future Sci. OA* **2015**, *1*, FSO30.
(80) Herbig, B.; Yu, X.; Diamond, S. Using Microfluidic Devices to Study Thrombosis in Pathological Blood Flows. *Biomicrofluidics* **2018**, *12*, 042201.
(81) Mottaghy, K.; Hahn, A. Interfacial Tension of Some Biological Fluids: A Comparative Study. *Clin. Chem. Lab. Med.* **1981**, *19*, 267−271.
(82) Phillips, R.; Kondev, J.; Theriot, J.; Garcia, H.; Orme, N. *Physical Biology of the Cell*, 2nd ed.; Garland Science, Taylor & Francis Group: New York, USA, 2013.
(83) Acharya, S. S.; Sarangi, S. N. In *Lanzkowsky's Manual of Pediatric Hematology and Oncology*, 6th ed.; Lanzkowsky, P., Lipton, J. M., Fish, J. D., Eds.; Academic Press: San Diego, USA, 2016; pp 279−333.
(84) Groot, R.; Warren, P. Dissipative Particle Dynamics: Bridging the Gap between Atomistic and Mesoscopic Simulation. *J. Chem. Phys.* **1997**, *107*, 4423−4435.
(85) Plimpton, S. Fast Parallel Algorithms for Short-Range Molecular Dynamcis. *J. Comput. Phys.* **1995**, *117*, 1−19.
(86) Groot, R.; Rabone, K. Mesoscopic Simulation of Cell Membrane Damage, Morphology Change and Rupture by Nonionic Surfactants. *Biophys. J.* **2001**, *81*, 725.
(87) Calvaresi, M.; Dallavalle, M.; Zerbetto, F. Wrapping Nanotubes with Micelles, Hemimicelles, and Cylindrical Micelles. *Small* **2009**, *5*, 2191−2198.
(88) Luu, X.-C.; Yu, J.; Striolo, A. Ellipsoidal Janus Nanoparticles Adsorbed at the Water-Oil Interface: Some Evidence of Emergent Behavior. *J. Phys. Chem. B* **2013**, *117*, 13922−13929.
(89) Partington, J.; Hudson, R. F.; Bagnall, K. Self-Diffusion of Aliphatic Alcohols. *Nature* **1952**, *169*, 583.
(90) Warren, P. Vapor-Liquid Coexistence in Many-Body Dissipative Particle Dynamics. *Phys. Rev. E: Stat. Phys., Plasmas, Fluids, Relat. Interdiscip. Top.* **2003**, *68*, 066702.
(91) Fan, H.; Striolo, A. Mechanistic Study of Droplets Coalescence in Pickering Emulsions. *Soft Matter* **2012**, *8*, 9533−9538.
(92) Solc, K. Shape of a Random-Flight Chain. *J. Chem. Phys.* **1971**, *55*, 335.

https://doi.org/10.1021/acsnano.1c00955
ACS Nano XXXX, XXX, XXX−XXX